



**HAL**  
open science

## MRI-based Imaging and Tracking of an Untethered Ferromagnetic Microcapsule Navigating in Liquid

Christian Dahmen, Karim Belharet, David Folio, Antoine Ferreira, Sergej Fatikow

► **To cite this version:**

Christian Dahmen, Karim Belharet, David Folio, Antoine Ferreira, Sergej Fatikow. MRI-based Imaging and Tracking of an Untethered Ferromagnetic Microcapsule Navigating in Liquid. *International Journal of Optomechatronics*, 2016, 10 (2), pp.73-96. 10.1080/15599612.2016.1166305 . hal-01305963v2

**HAL Id: hal-01305963**

**<https://hal.science/hal-01305963v2>**

Submitted on 21 Jul 2017

**HAL** is a multi-disciplinary open access archive for the deposit and dissemination of scientific research documents, whether they are published or not. The documents may come from teaching and research institutions in France or abroad, or from public or private research centers.

L'archive ouverte pluridisciplinaire **HAL**, est destinée au dépôt et à la diffusion de documents scientifiques de niveau recherche, publiés ou non, émanant des établissements d'enseignement et de recherche français ou étrangers, des laboratoires publics ou privés.

# MRI-based Imaging and Tracking of an Untethered Ferromagnetic Microcapsule Navigating in Liquid

Christian Dahmen, Karim Belharet, David Folio, Antoine Ferreira and Sergej Fatikow

**Abstract**—The propulsion of **ferromagnetic** objects by means of MRI gradients is a promising approach to enable new forms of therapy. In this work, necessary techniques are presented to make this approach work. This includes path planning algorithms working on MRI data, ferromagnetic artifact imaging and a tracking algorithm which delivers position feedback for the **ferromagnetic objects** and a propulsion sequence to enable interleaved magnetic propulsion and imaging. Using a dedicated software environment integrating path-planning methods and real-time tracking, a clinical MRI system is adapted to provide this new functionality for controlled interventional targeted therapeutic applications. Through MRI-based sensing analysis, this paper aims to propose a framework to plan a robust pathway to enhance the navigation ability to reach deep locations in human body. The proposed approaches are validated with different experiments.

**Index Terms**—Microrobotics, MRI-based sensing, navigation, path planning, visual tracking.

## I. INTRODUCTION

MRI is a powerful technology for diagnostics and widely used throughout the world. Some approaches to use MRI systems for assisting therapeutical approaches are existent, and new approaches are researched by many research groups. Robotics is an important topic in these approaches. Mostly the MRI is utilized in these cases as a means of sensory feedback for the procedure, whether it is robotics or manual action (see e.g. [1] for sensory feedback on intervention needle shape and deflection or [2] for the tracking of MRI-compatible devices). Also, much effort is spent into developing actuators and systems which are compatible with the special conditions inside the MRI system, specifically the strong magnetic fields. An overview and comparison can be found in [3], for details on a specific actuator see e.g. [4]. Using the MRI for sensory feedback though is not the only way the MRI can be used for therapeutic approaches.

Currently, Magnetic Resonance Imaging (MRI)-based medical microrobotic platforms are investigated to reach locations deep in the human body while enhancing targeting

This paper was presented in part at the IEEE International Conference on Intelligent Robotics and Systems, San Francisco, CA, September 25–29, 2011. This work was supported by European Union’s 7th Framework Program and its research area ICT-2007.3.6 Micro/nanosystems under the project NANOMA (Nano- Actuators and Nano-Sensors for Medical Applications).

C. Dahmen and S. Fatikow are with the Division Microrobotics and Control Engineering, University of Oldenburg, 26129 Oldenburg, Germany (Email: Christian.Dahmen@Informatik.uni-oldenburg.de; fatikow@uni-oldenburg.de).

K. Belharet is with the Laboratoire PRISME, Hautes Etudes d’Ingénieurs campus Centre, PRISME EA 4229, Bourges, France (Email: karim.belharet@hei.fr).

D. Folio and A. Ferreira are with the Laboratoire PRISME, INSA Centre Val de Loire, Université d’Orléans, PRISME EA 4229, Bourges, France (Email: david.folio@insa-cvl.fr; antoine.ferreira@insa-cvl.fr).

efficacy. This could be achieved using an upgraded clinical MRI scanner, and is referred as magnetic resonant navigation (MRN) [5]. Potential biomedical applications are targeting drug delivery in the brain [6], navigable magnetic carriers for implantable biosensors [7] or controlled ultrasensitive imaging for early diagnosis and treatment of diseases [8]. A recent breakthrough in interventional MRI-guided *in vivo* procedures demonstrated that real-time MRI systems can offer a well-suited integrated environment for the imaging, tracking, and control of a ferromagnetic device, which was done in the carotid artery of a living swine [9]. These successful experiments pointed out critical challenges in terms of real-time imaging, tracking and navigation for future therapeutic applications.

Dynamic tracking of ferromagnetic materials is mostly used due to significant magnetic susceptibility artifacts when present inside the MRI during imaging [10]. Moreover, image acquisition delays offer a great challenge for real-time interventional MRI. In [11], the authors demonstrate a new concept of magnetic signature selective excitation tracking (MS-SET) providing high position update rate. However, the poor position accuracy of the MS-SET tracking technique induces navigation or trajectory control errors over pre-planned paths [12]. Recently, in [13] an extension of this approach allows tracking ferromagnetic materials by generating RF-selective signatures with satisfactory localization accuracy and a reduction of the contrast-to-noise ratio (CNR). In contrast, few works address the robust navigation planning problem, that in our context is dealing with the MRI constraints [14]. As improvement, this paper reports on the MRI-based planning and sensing of micro/nano-devices aiming to navigate within vessels. More precisely, the motivation of this paper is to propose a framework to plan a *robust* pathway, wrt. MRI-based tracking capabilities to enhance the navigation ability to reach deep locations in the human body. Through a specially developed software environment integrating path-planning methods and real-time tracking, a clinical **Magnetom Verio 3T platform (Siemens, Germany)** MRI system is adapted to provide new functionality for potential controlled interventional targeted therapeutic applications. Specifically, this paper reports on the theoretical MRI-based tracking and navigation algorithms. An experimental study was conducted in order to assess the validity of the adapted clinical MRI software environment. **The MRI-data are used (i) to plan navigation path, (ii) to generate propulsion sequence with interleaved magnetic imaging and actuation and (iii) to track ferromagnetic micro-objects.**

The paper is organized as follows. We first describe the experimental setup using a clinical MRI System. **Section III de-**

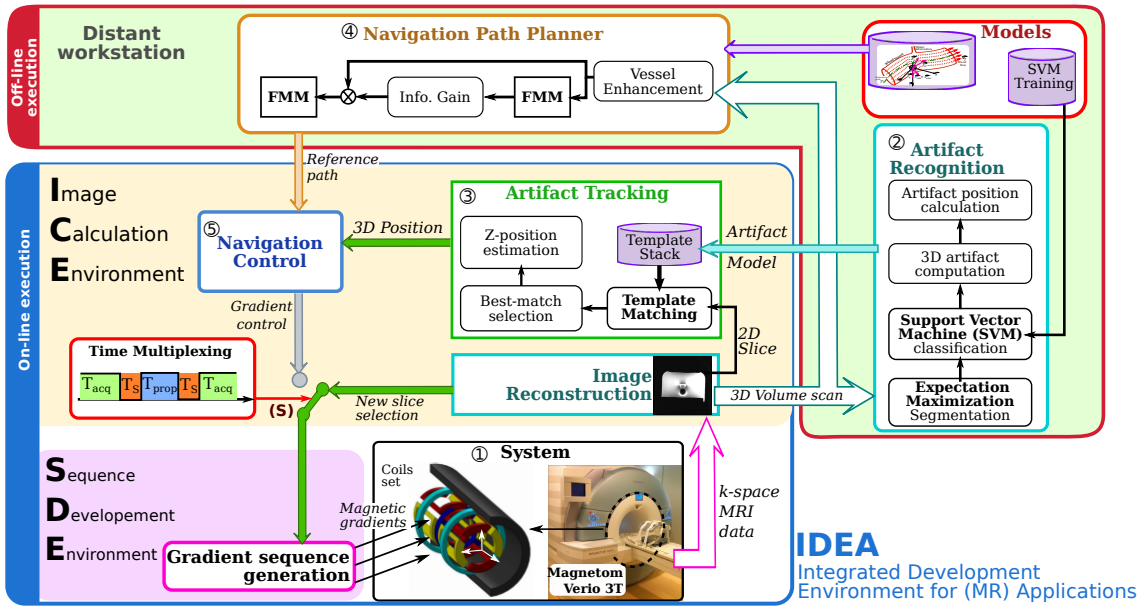


Fig. 1. The clinical MRI overall architecture: ① clinical Magnetom<sup>®</sup> Verio 3T (Siemens, Germany) MRI scanner; ② recognition; ③ tracking; ④ planning; and ⑤ navigation control modules.

describes the MRI artifact imaging and tracking for the magnetic microcapsule. Then, Section IV introduces the navigation path planning approach. Finally, Section V illustrates the efficiency of developed methodologies in magnetic resonance navigation.

## II. EXPERIMENTAL MRI SYSTEM

### A. MRI Setup Description

The Fig. 1 describes the overall architecture of the MRI-based microrobotic platform. A clinical Magnetom Verio 3T platform ① (Siemens, Germany) is used here for planning, imaging, tracking and propulsion of a microcarrier. These different functionalities are embedded in the Siemens MRI software environment IDEA<sup>1</sup> which comprises the ICE (Image Calculation Environment) where the algorithms are integrated, and the SDE (Sequence Development Environment) that generates the gradient sequence, as shown in Fig. 1. MRI-based navigation system requires observation of the scene in order to either plan the trajectory by off-line mapping, or to correct the device pose error on-line between the planned and the observed trajectory. To ensure a smooth conveyance of the capsule to its destination, while avoiding collisions and the risk to be trapped in wrong pathways, navigation performance will be affected by external perturbations and MRI technological constraints (such as nonnegligible pulsatile flow, limitations on the magnetic gradient amplitude, MRI overheating avoidance, etc.) [14]. Hence, to observe the device from the MRI-data, the sensing part comprises artifact recognition ② and tracking ③, which are presented in Section III. A control module ⑤ generates the magnetic gradient field to propel the microcarrier. Different control schemes have been successfully tested, such

as proportional-integral-derivative (PID) controller [15], predictive controller [16] or adaptive backstepping controller [17]. Moreover, the overall concept of the MRI-tracking system is based on the fact that both tracking and propulsion are possible with the manufacturer-supplied gradient coils of the MRI system. As illustrated in Fig. 1, the switch 'S' connected to the time-multiplexing block controls the interleaved magnetic imaging and propulsion sequences. Actually, at any instant only one of the functions could be applied (i.e. either tracking or propulsion), but both will be executed over the same MRI interface. The MRI system has therefore to be shared and a time-division-multiple-access scheme has been developed. Thus, the MRI time cycle is decomposed as follows:

$$T_{\text{Cycle}} = T_{\text{Acq}} + T_{\text{Prop}} + T_{\text{S}} \quad (1)$$

where  $T_{\text{Acq}}$ ,  $T_{\text{Prop}}$  and  $T_{\text{S}}$  are respectively the acquisition, propulsion and synchronization event time steps. The cycle time  $T_{\text{Cycle}}$  should be sufficiently small to ensure good stability and robustness of the control loop. In this work, we will focus our study on the planning and sensing processes.

### B. Software Integration

The MRI scanner is used to achieve sensing and propulsion using the existing gradient coils. The gradient system is a set of magnetic coils, which allows the generation of magnetic gradients in the 3D space within the MRI bore. In the experiments, a gradient strength of 20 mT/m is used, but it can be settled up to 40 mT/m. These gradients normally are used to achieve spatial encoding of the radio-frequency (RF) echo of the excited molecules. To generate propulsion forces, the gradients have to be switched into the direction of the desired motion. As the same coils have to be used for imaging and propulsion, an interleaved mode has been developed.

<sup>1</sup>IDEA: Integrated Development Environment for (MR) Applications, <https://www.mr-idea.com>

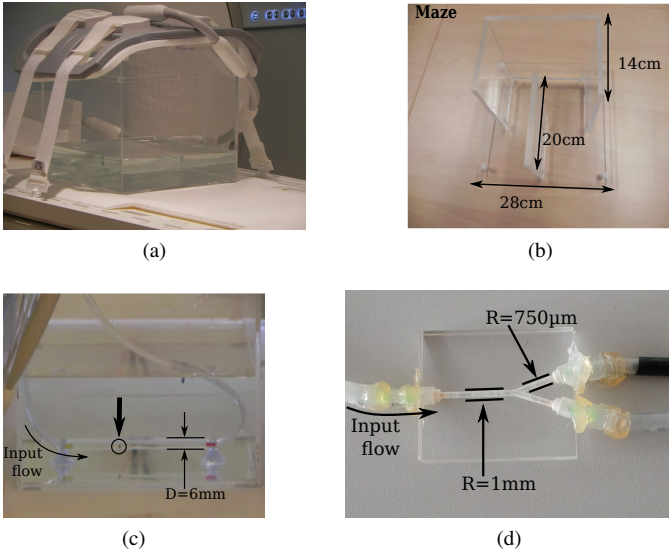


Fig. 2. The different experimental setups: (a) the square acrylic box that contains the different environment which is (b) a maze, (c) a channel, and (d) a Y-shaped microchannel.

The propulsion sequences are integrated in the IDEA software environment. Standard available imaging sequences are extended to include a controllable gradient in an adjustable direction in the SDE module. The magnetic gradient is switched before the imaging sequence is initiated. It allows a controller to generate gradient values from a previous feedback extracted from the last scanned image. The sequence receives input from the ICE module where image processing and controller are implemented (see Fig. 1). Depending on the input, the sequence duration and shape is calculated and applied. The duration can be set between several milliseconds to several seconds.

### C. Experiments Context

To conduct the various experiments presented in this paper a sealed cube shaped acrylic box was put into the bore of the clinical MRI platform, as shown in Fig. 2a. This acrylic box could embed different environment which is this study a maze (Fig. 2b), a straight channel (Fig. 2c) connected to a pulsatile pump (Harvard corporation, Washington, FL), and a Y-shaped microchannel (Fig. 2d). Finally, steel balls of different sizes were used and placed in the aforementioned environment.

## III. MRI-BASED SENSING

To enable efficient magnetic resonant navigation (MRN) a fast and accurate localization algorithm is required. Several approaches of MR-tracking have been developed which are commonly referred as active and passive techniques. Active tracking involves that small RF coils have to be attached to the device. While passive tracking markers need to be embedded [13], [18]. Here, the presence of ferromagnetic material acts as a passive marker [11], [13]. Specifically, local susceptibility difference causes a magnetic field distortion, namely a magnetic artifact. In this section, we first introduce the artifact imaging before presenting the artifact recognition

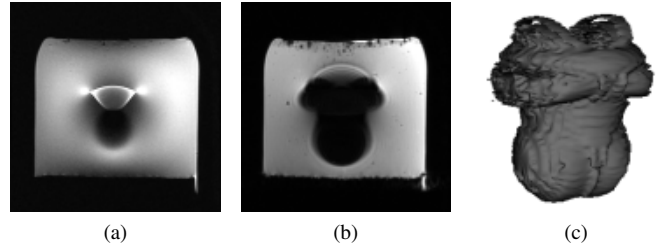


Fig. 3. MRI susceptibility artifact imaging experiment. Results for a 2.5 mm steel sphere, embedded into agarose gel: (a) conventional spin echo (SE) sequence; (b) conventional gradient echo (GE) sequence; and (c) reconstructed artifact volume of GE.

procedure. This knowledge helps to design a MR-tracking based on template matching.

### A. MRI susceptibility artifact imaging

Since the beginning of MRI, the occurrence of magnetic susceptibility artifacts has been studied. In clinical practice, the focus is usually on avoiding artifacts and producing correct images of anatomical structure [19]. The image acquisition procedure applied in MRI relies on the presence of a strong homogeneous magnetic field  $B_0$  and three well-defined magnetic gradients. Insertion of ferromagnetic material into the field of view clearly violates the assumption of homogeneity, leading to:

- 1) *Intravoxel Dephasing*: Spins inside a single voxel are dephased due to field inhomogeneity, this leads to a damping or loss of signal.
- 2) *Spatial misregistration*: The spatial coding scheme is corrupted and signals are registered incorrectly, causing bright fringes around metallic objects.

An actual artifact shape depends on several factors related to the magnetic object and the imaging sequence. Saturation magnetization and object volume are the most important object specific parameters. For small aspect ratios, object shape is of minor importance. The most important sequence dependent parameters are echo type (gradient echo or spin echo) and echo time. Generally, gradient echo (GE) sequences produce much larger artifacts than spin echo (SE) sequences, in terms of affected volume. This is due to their inability to compensate temporally constant field inhomogeneities.

In the developed system, susceptibility artifacts caused by ferromagnetic device is exploited for position determination. For this purpose, the imaging parameters and artifact formation principles are presented in the following.

### B. Artifact Recognition

The recognition of the artifact consists of an initial image segmentation followed by feature-based object recognition. For segmentation, the Expectation Maximization (EM) algorithm [20] with Gaussian mixture model has been selected as it has shown good results in many applications of medical image processing and is one of the most widely-used. Based on the raw segmentation, connected objects are detected. Shape- and pixel statistics features are extracted from each object and

serve as input to a Support Vector Machine (SVM) classifier. The SVM classifier must be trained for each sequence and object used. From the recognized artifact, the magnetic object location is calculated from the center of gravity and a fixed 3D displacement. The main goal of the classification procedure is to detect the artifact caused by the magnetic particle and to reject cavities or other anatomical structure obtained by the segmentation.

First, the imaging parameters have been studied (for details see [21]). A 2 mm steel sphere has been embedded into a 2000 ml container of agarose gel which produces a homogeneous background signal. A representative selection of imaging sequences has been tested: conventional gradient echo (GE) and conventional spin echo (SE) sequences. Sample scans taken from the imaging experiments and the segmentation results for the GE sequence can be seen in Fig. 3. The artifact observed in the GE sequence shows the highest dimensions. Highest signal peaks are found using the conventional SE sequence. It has to be noted, that the artifact dimensions are orders of magnitude above the object dimensions. From the segmented susceptibility artifacts centroid, the object location can be characterized using a fixed offset vector. The offset vector is derived from simulation of the MRI imaging process with the sequence type, parameters and object type. This position serves as the initialization of the localization for the tracking procedure described in the following section.

### C. Artifact Tracking

Our objective here is to track accurately the position of ferromagnetic microdevice either in 2D or 3D. Due to the characteristic shape of the artifact (see Fig. 3), we propose to localize the device using template matching procedure. To do so, during the recognition phase a template  $T$  is extracted which is subsequently be used for tracking. The chosen template matching approach is based on correlation:

$$C(x, y) = T(x, y) \star I(x, y) \quad (2)$$

with  $C(x, y)$  the correlation result matrix,  $\star$  the correlation operator and  $T(x, y)$  the template. The position of the artifact depicted in the template is then derived from the maximum position inside the correlation matrix:  $C(x_{\text{obj}}, y_{\text{obj}}) = \max(C)$ . The position of the maximal value in the correlation matrix corresponds to the position of the tracked object, and the center of gravity of the object can be computed.

To determine the 3D position of the artifact corresponding to the device, a correlation is applied with a template stack to deliver the third dimension coordinate. The approach used involves multiple correlation templates, which will be subsequently used and the best match determined. If the template stack contains a number of templates  $T_{1..n}$ , therefore, a number of correlation matrices  $C_{1..n}$  are also calculated. The best matching slice  $m$  is determined by:

$$\max(C_m) \geq \max(C_i) \quad \forall i \in (1..n) \quad (3)$$

The distance of the ferromagnetic object to the current slice position is determined in 3D. Specifically, the z-coordinate is extracted from the known matched template position relative

to the center template slice  $\Delta z(T_m)$  and the known scanned slice position  $z(I)$ . It can be noticed, that the sequence chosen has asymmetric characteristics, and a unique solution for this problem exists.

$$z_p = z(I) + \Delta z(T_m) \quad (4)$$

For speeding up the algorithm, image reconstruction may be skipped and the correlation directly executed in k-space. This is possible due to the correspondency of correlation in frequency domain:

$$T(x) \star I(x) \longrightarrow T(k) \cdot I(k) \quad (5)$$

The execution of the algorithm in k-space also enables the use of partially acquired k-space data (like the MS-SET approach). This leads to speeding up the acquisition time,  $T_{\text{Acq}}$ , because less iterations of the MRI sequences have to be executed.

The overall principle of the proposed algorithm can be seen in the module ②-③ in Fig. 1. A comparison with the MS-SET approach is proposed in Section VI.

### D. Tracking Performance

Several factors have influence on the accuracy, precision and duration of the overall tracking algorithms. The mains factors are:

- 1) MR sequence;
- 2) imaging noise;
- 3) k-space reduction;
- 4) artifact distortions due to changes in the environment (such as anatomical structures, etc.).

Basically, the algorithm could be speeding up thanks to k-space reduction, but also by using ultra-fast MR-sequences. For instance, from the Siemens MRI scanner, ultra-fast SE is obtained with half-Fourier acquisition single-shot turbo spin-echo (HASTE) sequence; and ultra-fast GE with fast low angle shot (FLASH) sequence. In the following, the influence of imaging noise and k-space reduction is further investigated.

1) *Imaging Noise*: If there is an ideal noise-free image  $I_n$  with additive noise  $I_s$ , the resulting image is obviously the sum of both:  $I = I_s + I_n$ . The additive noise may then lead to additional noise on the output of the algorithm, and on the extracted position. The correlation of a template  $T$  without noise with the noisy image will result in a signal related part  $C_s$  and a noise related part  $C_n$ :

$$C = T \star (I_s + I_n) = T \star I_s + T \star I_n = C_s + C_n \quad (6)$$

Therefore, if the images contains an increased level of noise and through this a lower signal-to-noise ratio (SNR), the SNR of the correlation function decreases as well. This is not problematic as long as the determination of the maximum is still possible without ambiguities. Until this happens, the output data, the position of the found template, will not be altered by additional noise. The confidence score generated by the algorithm will decrease. The confidence score of the algorithm is a measure for the determined similarity of the used template and the area surrounding the determined position.

In the experiments conducted on the MRI scanner, the acquired images have been used to evaluate the noise characteristic. Therefore, 100 images have been evaluated and analyzed. The difference to the mean value has been computed. It appears that the noise follows a Gaussian distribution, with a standard deviation of  $\sigma = 17.7$ . Therefore, it can be assumed for the scope of this paper that the noise influence can be modeled using Additive White Gaussian Noise (AWGN).

2) *The k-space Reduction* : The effect of k-space reduction on the algorithm performance has been estimated. The k-space reduction means that a certain amount of data in k-space is not acquired and therefore set to zero. If a template  $T$  is correlated with an image with missing data, the effect is the same like a correlation with a template with missing data. This can be derived from the correspondence in k-space (5), that leads with an image with reduced k-space to:

$$T(k) \cdot I_r(k) = M_r \cdot T(k) \cdot I(k) \quad (7)$$

with  $M_r$  the matrix used to "virtually" zero out parts of k-space. The reduction in k-space to only one line and column reduces the features of any object depicted. The resulting image is in effect the overlay of two one-dimensional signals. These two signals can be separated:

$$M_r \cdot T(k) \cdot I(k) \rightarrow T_x(k) \cdot I_x(k) \wedge T_y(k) \cdot I_y(k) \quad (8)$$

Therefore, a feature which can be detected and its position determined in each dimension separately, can be detected in an image with reduced k-space.

Due to the fact that the GE-like sequences used image artifacts as very pronounced signal losses, the detection of these artifacts is possible in k-space reduced images. Even if the detection is not possible in one separate dimension, a correlation between the two signals will in most cases deliver the position. The detectability is limited by the noise on the signal and the size of the signal loss.

### E. MR-Tracking Evaluation Results

The accuracy of implemented MRI-based sensing has been evaluated in several experiments with different setups. The experiments have been realized to evaluate the tracking uncertainties, the influence of noise and of k-space reduction on the tracking algorithm performance. The relevant MR-imaging parameters are given in Table I. Experimental results are described in the following.

TABLE I  
MR-IMAGING PARAMETERS

Parameter	Value
Repetition time $T_r$	7.5 ms
Echo time $T_e$	4.1 ms
Slice thickness	5 mm
k-space resolution	$192 \times 192$
Image matrix	$256 \times 256$
FOV	400mm
GE and FLASH flip angle $\alpha$	$15^\circ$

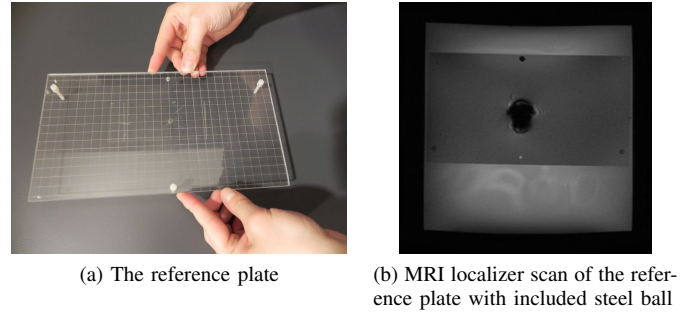


Fig. 4. Structured acrylic plate for tracking performance characterization.

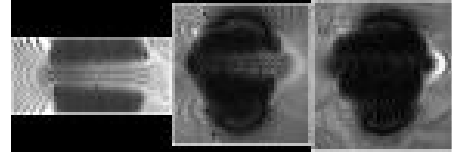


Fig. 5. Samples of templates used for the MR-tracking procedure with FLASH sequence.

1) *Tracking Results*: To evaluate the efficiency of the tracking algorithm, experiments have been executed using a clinical Magnetom Verio 3T platform (Siemens, Germany) MRI scanner. Steel ball was fixed at a defined position on a structured acrylic plate with the dimensions of  $280 \text{ mm} \times 154 \text{ mm}$ , as illustrated in Fig. 4a. A regular grid of 10 mm is drawn on the structured plate. 100 MR-slices have been acquired of the same steel sphere position. Examples of the templates used for the MR-tracking procedure are shown in Fig. 5. The tracking process uncertainty has been evaluated, in order to quantify the 2D localization within a MR-slice. To do so, steel balls of different sizes (ranging from 0.7 mm to 3.0 mm) have been used and repeatedly scanned in static case. The imaging sequences used for this were a HASTE and a FLASH sequence with the MRI parameters given in Table I. The corresponding results are summarized in table II. It can be seen, that the standard deviation ( $\sigma_x$  and  $\sigma_y$ ) of the extracted 2D location is mostly better when using the FLASH sequence. No clear dependency on size can be observed. Generally, the standard deviation lies well below  $200 \mu\text{m}$ .

Secondly, the 3D tracking algorithm efficiency has been evaluated. Once again, 100 MRI acquisitions have been recorded to evaluate the uncertainty. In the worst case, when SE-like sequences are used, the standard deviation is less than  $\sigma_z < 30 \mu\text{m}$ . Basically, the accuracy of the  $z$ -coordinate is mainly related inter-slice distance  $d$ , and is below  $0.01 \times d$ .

2) *Determination of Imaging Noise Influence*: To evaluate the influence of noise a 1 mm steel ball has been fixed at a defined position on the structured acrylic plate (see Fig. 4a). The MR-data are compared with the known data on the steel sphere position. The variation in sensor data output between images was observed. The resulting MRI image can be seen in Fig. 4b. The experiments showed no relevant variation of the extracted data, with the standard deviation being 0.1 pixels in  $x$ -direction and zero in  $y$ -direction. One reason for the standard deviation being zero is that the algorithms are only pixel-exact, and the noise generated would affect the output data to a lesser

TABLE II  
STANDARD DEVIATIONS IN X ( $\sigma_x$ ) AND Y ( $\sigma_y$ ) DIRECTIONS FOR THE TRACKING ALGORITHM

Size (mm)	Sequence	$\sigma_x$ (voxels)	$\sigma_y$ (voxels)	$\sigma_x$ (mm)	$\sigma_y$ (mm)
0.7	HASTE	0.080	0.043	0.100	0.053
1.0	HASTE	0.097	0.074	0.122	0.092
1.5	HASTE	0.127	0.127	0.159	0.159
2.0	HASTE	0.116	0.098	0.144	0.123
3.0	HASTE	0.042	0.044	0.053	0.055
0.7	FLASH	0.038	0.056	0.043	0.064
1.0	FLASH	0.035	0.054	0.042	0.063
1.5	FLASH	0.036	0.054	0.042	0.063
2.0	FLASH	0.047	0.061	0.055	0.071
3.0	FLASH	0.166	0.158	0.194	0.185

extent than the algorithm resolution.

3) *K-Space Reduction*: To evaluate the algorithm performance with reduced k-space data during reconstruction, only a subset of lines and columns in k-space is used for image reconstruction before the algorithm execution. For the sake of illustration, images recorded with the MRI are transformed, then the k-space reduced, before transforming back to image space. The images have an initial resolution of  $192 \times 192$  pixels; and the number of used k-space lines and columns respectively are 1, 2, 3, 4, 5, 10 and all 192. Hereafter, different experiments are described.

a) *Gradient echo-like sequence*: First, FLASH sequence is considered, and the reference plate setup shown in Fig. 4a is used with a 1 mm steel ball fixed at a defined position. The corresponding k-space reduction is depicted in Fig. 6. As one can see, the effect of the reduced k-space data is the decreasing detail of the artifact. The principal position and extent of the artifact is still visible and detectable.

The standard deviation estimations from the 100 MR-slice images are summarized in Table III. It appears an increase of the standard deviation for the strongly reduced k-spaces. However, the position determination is still possible and relatively robust, even with only one k-space line and column. This results are consistent with the MS-SET approach with a similar average error [11]. Here, the standard deviation increases if less than 5 rows and columns are acquired. Therefore, an increase of the k-space data does not significantly improve the MR-tracking accuracy.

TABLE III  
STANDARD DEVIATION OF THE DETERMINED POSITION DURING ANALYSIS OF THE 100 SLICE IMAGES OF THE REFERENCE PLATE FOR DIFFERENT K-SPACE REDUCTIONS

n	x-pos [mm]	std(x) [mm]	y-pos [mm]	std(y) [mm]
1	143.81	0.493	132.8	0
2	143.8	0.47	132.8	0
3	143.78	0.31	132.8	0
4	143.77	0.156	132.8	0
5	143.77	0.156	132.8	0
10	143.77	0.156	132.8	0
all	143.77	0.156	132.8	0

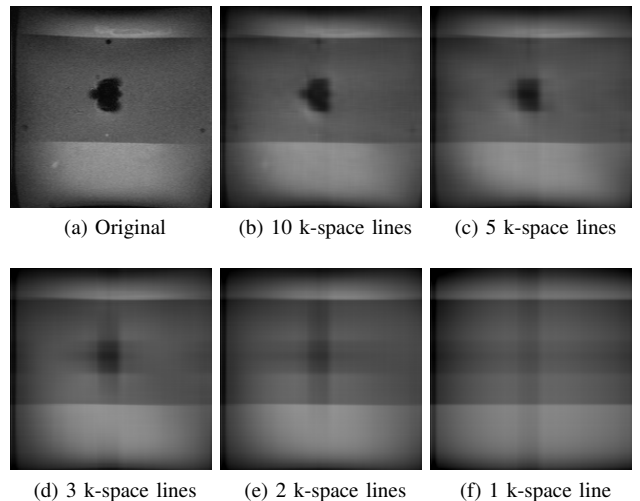


Fig. 6. Images reconstructed with reduced k-space data using is FLASH sequence.

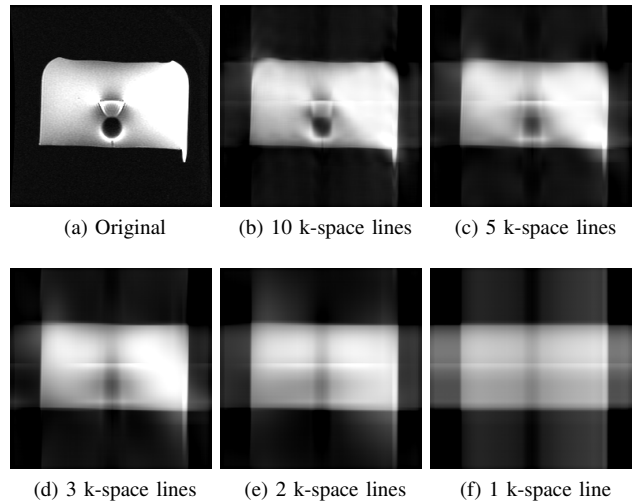


Fig. 7. Images reconstructed with reduced k-space data using a SE sequence.

b) *Spin echo-like sequence*: In case of a SE-like sequence, the same effect can be observed when the k-space is reduced. In Fig. 7, a 1 mm steel ball was imaged using a conventional SE sequence. It can be observed that the dark regions of the artifact are less pronounced, and therefore less detectable in the heavily reduced k-space images.

c) *Moving object*: Using the k-space reduction, steel balls have been moved using the MRI magnetic gradients, and its motion tracked in the MRI data. The sequence used here was a conventional GE sequence. Fig. 8a shows the evolution of moving object. These results exhibit the feasibility to track a moving particle even with a reduced k-space. Especially, the k-space reduction does not change significantly the tracking results.

With a 1 mm steel ball and slice stack imaging, the size of the determined artifact can be determined in dependence of the slice position and the k-space reduction. The result for a GE sequence can be seen in Fig. 8b. It can be concluded that given a known artifact size in the center slice, the out-of-

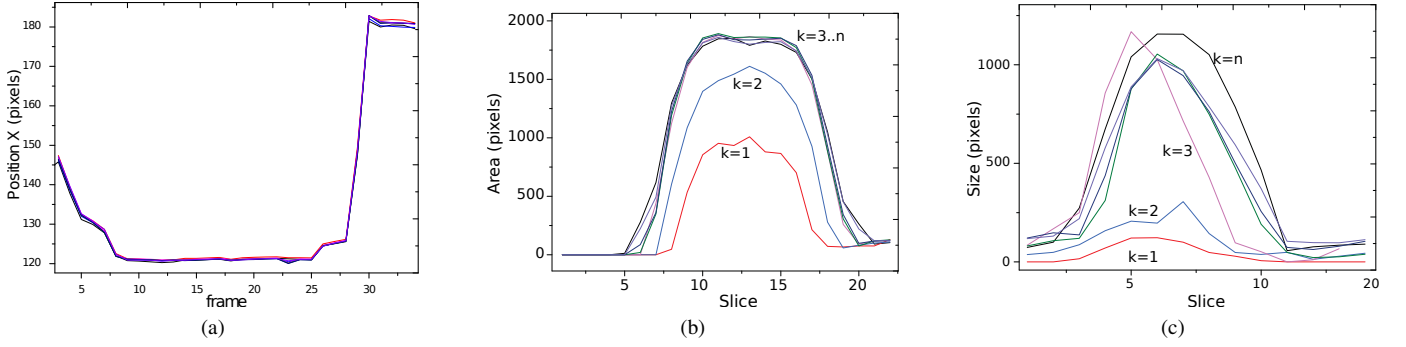


Fig. 8. MR-Tracking of a moving device. (a) Evolution of moving particle. (b) The area of the artifact inside the image in dependency from slice and k-space reduction with a GE sequence and a 1 mm steel ball. (c) Size of the artifact inside the image in dependency from slice and k-space reduction with an SE sequence and a 1 mm steel ball.

slice displacement of the artifact could be determined using the size information. This is even possible for heavy k-space reductions. Problematic is the identification of the displacement near the artifact center, because of only slightly changing size. This is better done using template stack matching and identification of the changing shape.

Similarly, using a 1 mm steel ball with a SE sequence, the size of the artifact can be seen in Fig. 8c. The possibility to use heavy k-space reductions is diminished. This is clearly because the overall size of the artifact is smaller and less dominated by areas of signal loss. In this case, only template stack matching or similar algorithms can deliver valid results on full k-space filled images.

4) *Final Statement:* From the above evaluation of the developed MR-tracking procedure based on template matching, it appears that GE-like sequences offer better tracking performance rather than SE-like sequences. Therefore, in the following only the FLASH (an ultrafast GE sequence) imaging sequence is retained.

#### IV. ROBUST NAVIGATION PLANNING WITH UNCERTAINTY

To allow a carrier to navigate properly within a tubular structure network we need to find a valid pathway between a initial and final states. In this section a navigation path planning robust to MR-sensing is presented.

##### A. Fast Marching Path Planning

In previous works [16], [22], we have proposed a framework allowing finding a minimal centered navigation path build upon the Fast Marching Method (FMM) firstly introduced by Sethian [23]. In the FMM framework the path finding problem is solved through the computation of the minimal action map  $\mathcal{U} : \mathcal{C} \mapsto \mathbb{R}^+$ , associated to an initial point  $\mathbf{x}_0$  on a domain  $\mathcal{C} \subset \mathbb{R}^d$  (with  $d = 2$  or  $3$ ). Moreover, the map  $\mathcal{U}$  satisfies the Eikonal equation:

$$\begin{cases} \|\nabla \mathcal{U}(\mathbf{x})\| = w(\mathbf{x}), & \forall \mathbf{x} \in \mathcal{C} \\ \mathcal{U}(\mathbf{x}_0) = 0 \end{cases} \quad (9)$$

where the isotropic cost function  $w : \mathbf{x} \in \mathcal{C} \mapsto w(\mathbf{x}) \in \mathbb{R}^+$  is a metric; and the map  $\mathcal{U}$  is a weighted distance map to the source  $\mathbf{x}_0$ . Specifically,  $\mathcal{U}$  may be regarded as the arrival times

of a front propagation from the source with velocity  $1/w(\mathbf{x})$ . As this map  $\mathcal{U}$  has only one local minimum: the point  $\mathbf{x}_0$ , the minimal path can be retrieved with a simple gradient descent on  $\mathcal{U}$  from a targeted seed  $\mathbf{x}_f$  to  $\mathbf{x}_0$ . The key issue of the FMM is then to define an appropriate and efficient cost function  $w(\mathbf{x})$  which drives the front propagation efficiently. A basic idea is to design such cost function on spatial consideration, that leads to:

$$w_{\text{Tub}} : \mathbf{x} \in \mathcal{C} \mapsto \text{Enhance}(\mathbf{x}) \in \mathbb{R}^+ \quad (10)$$

where  $\mathcal{C}$  is the input MRI data, and  $\text{Enhance}(\mathbf{x})$  is a tubelike enhancement function. To design  $\text{Enhance}(\mathbf{x})$  we use some *a priori* knowledge about tubiform shape and intensity in MRI data. Hence, a typical cost function  $w_{\text{Tub}}$  could be simply designed by using a multi-scale analysis based on geometric properties of the image retrieved from the Hessian matrix. Such filter, proposed by Frangi [24] or Sato [25] allows computing a pseudo-probability of belonging to a tubular structure. We have applied this approach to different sets of data, in 2D [22] as well as in 3D [16]. However, designed solely on spatial consideration, the centerline geodesic does not take into account the sensing uncertainties.

##### B. Planning with MRI Uncertainties

There are several important sources of uncertainty which should be considered in MRI-based navigation planning. These include uncertainty in MRI data acquisition and processing, carrier model and position tracking. Failure to account for these uncertainty sources in the planning method could result in trapping the device in a wrong tube segment or collision with the environment obstacles. Therefore, explicitly modeling sensing uncertainty is a main key to robustness. In particular, in our context we have to ensure efficient sensing capability with a low level of uncertainty. For that, we simulate in real-time the microdevice's imaging and tracking process in order to assess each candidate configuration wrt. a sensing objective.

Thus, we aim to define a navigation path that maximizes the likelihood of successful execution by ensuring that sensor information can be gathered at all crucial stages during execution. Therefore, our motivation is then to define a new cost



function  $w_{\text{Bel}}$  that maps the system's belief in its position  $\mathbf{x}$  wrt. a sensor model, that is:

$$w_{\text{Bel}} : \mathbf{x} \in \mathcal{C} \mapsto \text{Bel}(\mathbf{x}) \in \mathbb{R}^+ \quad (11)$$

where  $\text{Bel}(\mathbf{x})$  is a measurement of the microrobot's belief in its state  $\mathbf{x}$ , that is the uncertainty. In the following paragraph, the basic strategies to model such metric  $w_{\text{Bel}}$  is presented.

1) *Dealing with Uncertainties*: Classically, when dealing with sensing uncertainty the most common approaches are based on probabilistic techniques, since these provide powerful statistical tools to manage noisy measurement. Those techniques usually rely on probabilistic models of the observation  $\mathbf{y}$  that take a *statical* interpretation of the underlying noise. Therefore, a variety of mathematical models for uncertainty of position information have been researched and proposed. For instance, Fox *et al.* [26] propose to relate the robot's belief to location uncertainty using Bayesian filtering. Bayesian filtering is one of the most robust methods of localization [26], in which a probability distribution:  $\text{Bel}(\mathbf{x}_k) = p(\mathbf{x}_k | \mathbf{y}_{1:k})$  is inferred over the (unknown) system state  $\mathbf{x}_k$  at time  $t_k$  following a series of noisy actions and measurements  $\mathbf{y}_{1:k}$ . However, such Bayesian filtering assumes that the dynamics of the device is known, which is classically difficult to establish. In this work, we do not consider such dynamic modeling. Furthermore, it has been recognized that the accuracy of the sensing action will commonly depend on the (micro-)robot location [27], [28], especially when using a MRI-based sensing system. Such mapping is often referred as Sensor Uncertainty Field (SUF) introduced in [29]. Elements of the SUF can be captured by incorporating some concepts from information theory [28], [30]. Information theory provides different tools such as entropy, the Kullback-Leibler divergence, and so on [31]. Hence, we propose to use the SUF formalism to define a mapping from a state  $\mathbf{x}$  to the expected information gain  $\mathcal{I}(\mathbf{x}; \mathbf{y})$ , that is (11):  $\mathbf{x} \in \mathcal{C} \mapsto \mathcal{I}(\mathbf{x}; \mathbf{y}) \in \mathbb{R}^+$ .

2) *Expected Information Gain as robot's belief*: The expected information gain (or, equivalently, the expected entropy reduction or mutual information) quantifies the microdevice's ability to localize itself at different positions  $\mathbf{x} \in \mathcal{C}$ : locations with high  $\mathcal{I}(\mathbf{x}; \mathbf{y})$  correspond to locations that generate sensor measurements  $\mathbf{y}$  that we expect to maximize the tracking process accuracy. Thus  $\mathcal{I}(\mathbf{x}; \mathbf{y})$  is computed, given an observed data  $\mathbf{y}$ , from the difference in Shannon entropy of the prior and posterior distributions:

$$\mathcal{I}(\mathbf{x}; \mathbf{y}) = H(\mathbf{x}) - H(\mathbf{x} | \mathbf{y}) \quad (12)$$

where the Shannon entropy  $H(\mathbf{x})$  of a probability distribution  $p(\mathbf{x})$  is defined as:  $H(\mathbf{x}) = - \int p(\mathbf{x}) \log p(\mathbf{x}) d\mathbf{x}$ . The prior entropy  $H(\mathbf{x})$  measures the carrier's belief of its position  $\mathbf{x}$  in  $\mathcal{C}$ , before the sensory input  $\mathbf{y}$  is received. The conditional entropy  $H(\mathbf{x} | \mathbf{y})$  denotes the expected entropy change after measurement data  $\mathbf{y}$ , and is given by:  $H(\mathbf{x} | \mathbf{y}) = H(\mathbf{x}, \mathbf{y}) - H(\mathbf{y})$ , where  $H(\mathbf{y})$  is the entropy of the likelihood  $p(\mathbf{y})$  of observing data  $\mathbf{y}$  and is calculated from the prior position distribution and the sensor model; and  $H(\mathbf{x}, \mathbf{y})$  is the joint entropy computed from the joint probability  $p(\mathbf{x}, \mathbf{y}) = p(\mathbf{y} | \mathbf{x})p(\mathbf{x})$ .  $p(\mathbf{y} | \mathbf{x})$  is the likelihood of sensing data  $\mathbf{y}$  at location  $\mathbf{x}$ , and is obtained from the sensor model and the observed scene. Finally, the path that

minimizes the uncertainty is then the one that maximizes the expected information gain  $\mathcal{I}(\mathbf{x}; \mathbf{y})$ .

### C. Application

We apply here the proposed navigation path planning to get a pathway that increase the belief in the microrobot position sensing. Thus, we have to first calculate the prior entropy  $H(\mathbf{x})$  that is related to a probabilistic model of the physical space. To this aim we use our *a priori* knowledge. In the case of pipe navigation, each (unknown) state  $\mathbf{x}$  must be within the tubular structures. Therefore, as previously introduced,  $\text{Enhance}(\mathbf{x})$  could be seen as a pseudo-probability for the device of belonging to a tubular structure, and leads to:  $p(\mathbf{x}) \propto \text{Enhance}(\mathbf{x})$ . The sensor model  $p(\mathbf{y} | \mathbf{x})$  could incorporate everything about the sensing objective, including SNR, detection probabilities, and whether the locations  $\mathbf{x}$  are visible. Here, to compute  $H(\mathbf{x} | \mathbf{y})$ , we assume that the sensing process could be modeled by a white multivariate-Gaussian distribution:  $\mathcal{N}(0, \Sigma_{\mathbf{y}}^2)$ , with zero mean and  $\Sigma_{\mathbf{y}}^2$  the covariance matrix. To evaluate the efficiency of our proposed approach, we have first considered a FLASH sequence tracking process of a 1 mm steel ball. Thus the covariance matrix  $\Sigma_{\mathbf{y}}^2$  of the Gaussian sensor model is computed using the table II, and is shown on Fig. 10. Finally a secondary FMM step is executed to get a pathway that maximizes  $\mathcal{I}(\mathbf{x}; \mathbf{y})$  within the tubular structure. This new navigation path extraction procedure is *robust* to uncertainties, and is illustrated in Fig. 1 in the navigation path-planner module.

Fig. 9.b shows the corresponding computed expected information gain  $\mathcal{I}(\mathbf{x}; \mathbf{y})$  and the resulting navigation path for the 1 mm steel ball tracking sequence. The obtained pathway between the selected points is then the one that minimize the sensing uncertainty during the navigation. To evaluate the consistency of the obtained pathway, we have computed the energy functional:  $\mathcal{E} = \sum_{\mathbf{x} \in \mathcal{P}} \mathcal{I}(\mathbf{x}; \mathbf{y})$  of each point along the computed path  $\mathcal{P}$ , and their geodesic length  $L$ . As one can see the pathway based on information gain  $w_{\text{Bel}}$  cost (Fig. 9.b) provides more energy and is smaller, than the one computed using the spatial  $w_{\text{Tub}}$  cost (Fig. 9.a).

Moreover, we have considered different Gaussian distribution  $\mathcal{N}(0, \Sigma_{\mathbf{y}}^2)$  within the sensor model, and applied our navigation path planner. The corresponding energy functional  $\mathcal{E}$  evolution wrt. different covariance matrix  $\Sigma_{\mathbf{y}}^2$  are illustrated on Fig.11. As expected, low  $\Sigma_{\mathbf{y}}^2$  leads to better energy  $\mathcal{E}$ , that is more information and certainty along the navigation path. Especially, for each information gain  $w_{\text{Bel}}$  cost computed different pathway has been obtained with different length, implying that the  $\mathcal{E}$  evolution are not monotonic.

Finally, the navigation path based only on uncertainty commonly overestimates the navigation path leading to inconsistencies such as e.g., tube wall contouring (as depicted on Fig. 9.b) or tube crossing. In such a case, a solution is to compute a weighted sum between the cost functions based on spatial information  $w_{\text{Tub}}$  and the one based on expected information gain  $w_{\text{Bel}}$ , that is:

$$w_{\text{Iso}} = \lambda_1 w_{\text{Tub}} + \lambda_2 w_{\text{Bel}} \quad (13)$$

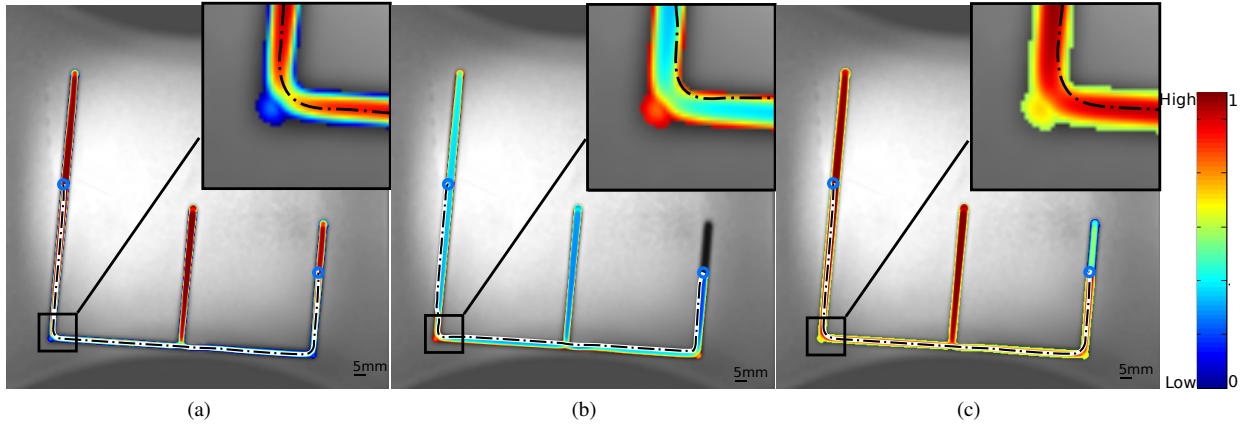


Fig. 9. Navigation path extracted using: a)  $w_{\text{Tub}}$  tubelike enhancement cost function (i.e.  $\text{Enhance}(\mathbf{x})$ ); b)  $w_{\text{Bel}}$  information gain cost function (i.e.  $\mathcal{I}(\mathbf{x}; \mathbf{y})$ ); c) weighted sum of the previous cost map  $w_{\text{Iso}}$  cost function.

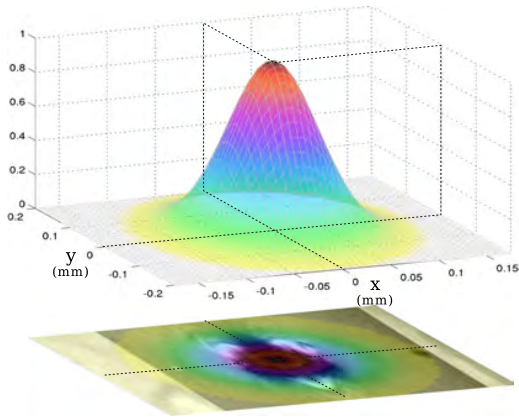


Fig. 10. Tracking process modeled as a white multivariate-Gaussian distribution.

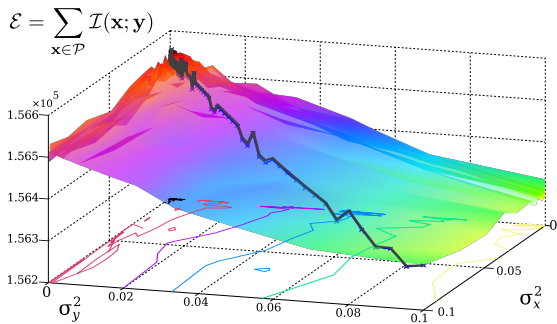


Fig. 11. Energy functional of the expected information wrt. the noise covariance.

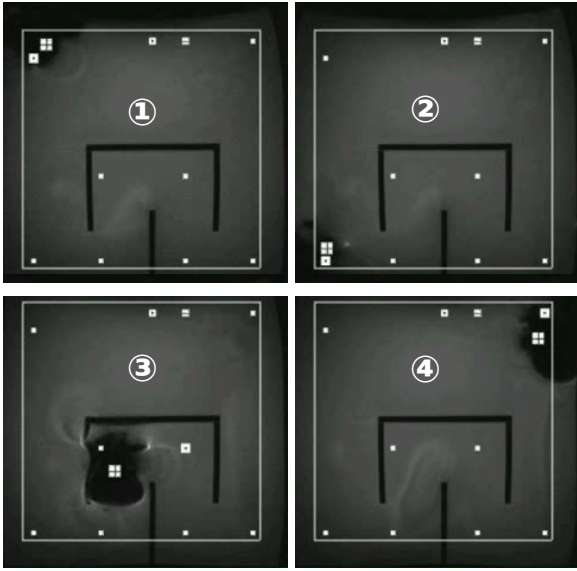
where  $\lambda_1$  and  $\lambda_2$  are weighting factors. Hence, this new isotropic cost function formulation allows to tune the navigation path to be either a centerline path or maximizing the expected information gain. The Fig. 9.c presents a pathway extracted using the isotropic cost function  $w_{\text{Iso}}$  computed with  $\lambda_1 = 0.6$  and  $\lambda_2 = 1 - \lambda_1$  from the  $w_{\text{Tub}}$  and  $w_{\text{Bel}}$  shown on Fig. 9.a and Fig. 9.b respectively.

## V. MAGNETIC RESONANT NAVIGATION RESULTS

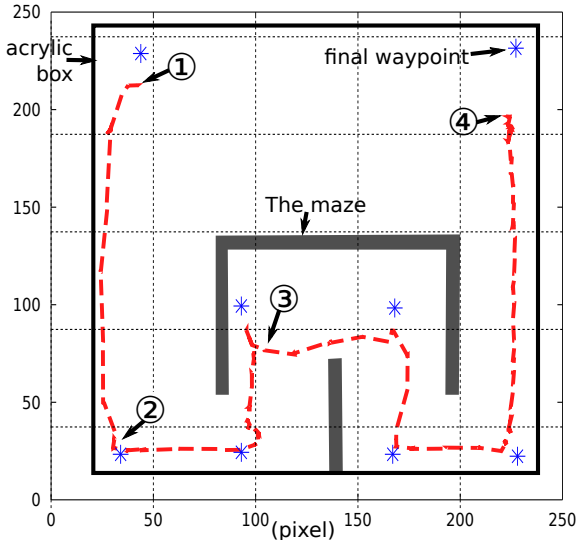
### A. Proof of Concept Validation

To evaluate the proposed MRI-based sensing and navigation procedure, we have first implemented a simple propulsion procedure within the clinical MRI system. The proposed sensing and navigation framework has been validated to follow a predefined path. To evaluate the timing behavior, the setup has been here restricted to 2D movements around a simple maze (see Fig.2b), and a capsule with a steel ball of  $750\mu\text{m}$  radius has been introduced into a closed box within the clinical MRI. As the environment is quite simple, the path is here decomposed through some waypoints (blue-marker in Fig. 12b and 13b). The imaging procedure use a FLASH sequence with a repetition time  $T_r = 9.1$  ms and an echo time  $T_e = 4.8$  ms. Hence, with full acquisition of the k-space of 256 lines, the total acquisition time is  $T_{\text{Acq}} = 2.33$  s. The propulsion time step has been set to  $T_{\text{Prop}} = 500$  ms. For the computation of the total duration of an imaging/propulsion loop, the gradient switching time also has to be taken into account. The gradient switching speed depends on the gradient strength and is limited by the maximal slope of the gradients which is  $\frac{dB}{dx dt} = 200$  T/m/s. Because only gradient strength  $< 20$  mT/m have been used, the synchronization time is then  $T_S = 200\mu\text{s}$ . Therefore, the total cycle time is  $T_{\text{Cycle}} < 3030$  ms. Notice that the values reported for  $T_{\text{Acq}}$  and  $T_S$  can be seen as upper boundaries. The MRI data of that experiment is illustrated in Fig. 12. The ferromagnetic capsule start from the location ① and have to follow the path to reach the final waypoint (above ④). These results demonstrate that the proposed MRI-based navigation is able to propel a device using a clinical MRI, even though with a high cycle time.

Furthermore, as previously introduced, the tracking of the artifacts can be executed using only a single imaged slice. Limited k-space reduction allows to further speed up the acquisition of the slices, while maintaining precision. Depending on the state of the capsule and the navigation difficulty, a trade off may be chosen between maximum accuracy while limiting speed, and maximizing the acquisition speed through complete k-space reduction which leads to lower accuracy.



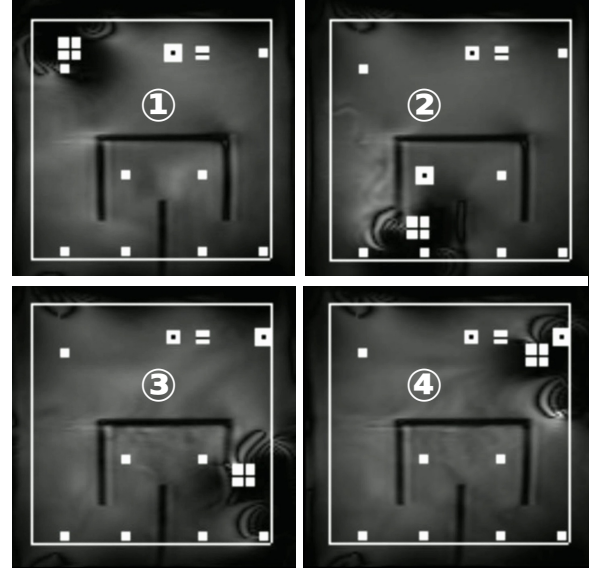
(a)



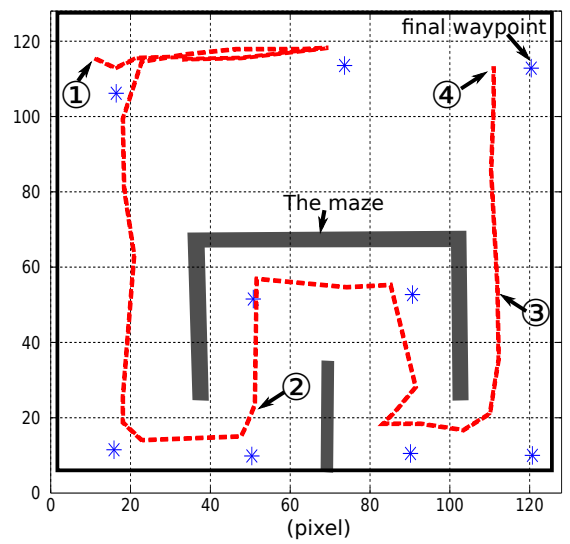
(b)

Fig. 12. Navigation along a planned path of a microcapsule with standard FLASH sequence: (a) some representatives MRI slice; and (b) the tracked path. The blue marker denotes the defined waypoints.

Especially,  $T_{Acq}$  is directly proportional to the number of k-space lines acquired. For this reason, reducing the number of k-space lines as it has been described above decreases  $T_{Acq}$  to  $\#lines/256$  of the original value. Let us notice that further speedup can be also achieved by reducing the repetition time  $T_r$  and echo time  $T_e$  accordingly. Fig. 13 illustrates a similar navigation task with improved imaging parameters with a repetition time  $T_r = 7.5$  ms and an echo time  $T_e = 4.8$  ms, and where the k-space is reduced to 128 lines. Thus, the total acquisition time is now  $T_{Acq} = 960$  ms, while the propulsion time is still  $T_{Prop} = 500$  ms. As one can see, in this case the magnetic device track more efficiently the desired trajectory. In particular, with a standard parameters set the capsule navigates in open-loop for a longer duration than the latter. Fig. 14 shows the error curve for the both cases. It appears clearly that the



(a)



(b)

Fig. 13. Navigation along a planned path of a microcapsule with optimized FLASH sequence parameters: (a) some representatives MRI slice; and (b) the tracked path.

optimized FLASH sequence is more efficient than the standard one. Moreover, a significant increase of the path tracking error appears when navigating close to the maze structure. These experiments depict the influence of the use of optimized MRI-sensing procedure to speed up the artifact tracking, and then improve the overall navigation. Indeed, the overall time execution in the first case is about 121 s and decrease to 40 s with optimized parameters.

Furthermore, this optimization step could be achieved by analyzing the sensing uncertainty in the navigation environment. Fig. 15 illustrates the information gain mentioned in Section.IV-B computed in the workspace. When the microcapsule navigates close to the maze obstacles, its artifact signature disturb the environment perception implying an increase of the sensing uncertainty. Thus, in vicinity of the maze the belief in the artifact location is low, and it remains difficult to track it.

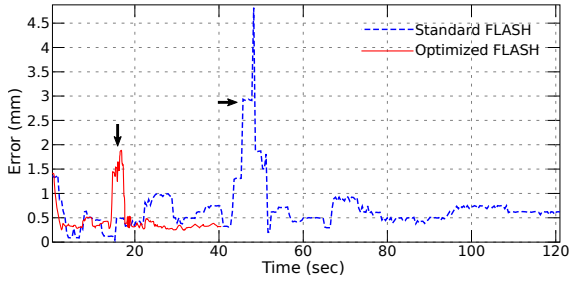


Fig. 14. Path tracking error when using standard and optimized FLASH sequences. The black arrow indicates the maze crossing.

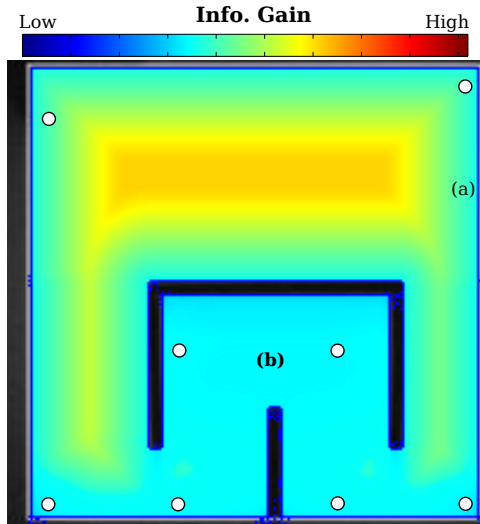


Fig. 15.  $w_{Be1}$  information gain cost function computed in the maze workspace.

### B. Channel Navigation

For realistic experiments, we used various vascular simulators filled with a viscous fluid (80% water and 20% glycerin) mimicking flow viscosity, and put into the bore of the clinical MRI platform. An open supply fluid reservoir was connected to a computer-controlled systolic pump simulating heart beating cycles (Harvard corporation, Washington, FL). Positioning tracking and control of the capsule robot moving in a channel is experimentally evaluated using a PID feedback controller for various mm- and  $\mu$ m-sized fluidic channels.

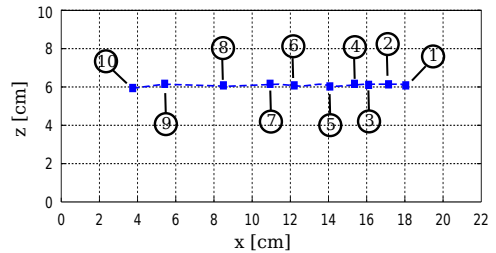
#### 1) Navigation in a millimeter-sized vessel simulator:

Fig. 2c shows the mm-sized vascular simulator inserted into the bore of the MRI scanner. A ferromagnetic bead of 1 mm of diameter is placed in a straight acrylic channel with an inner radius of 3 mm. The Harvard pulsating pump has the following three variables for the control of the pulsating flow. The parameters are: (i) the ratio of systole/diastole (fixed at 25/75%), (ii) the pulsating rate of the pump, and (iii) the flow rate per stroke. Different flow rates are considered:

a) *Steady flow:* For the experiments, the flow rate per stroke was settled at a low value (steady flow conditions) with a pulsating rate leading to a mean flow velocity of 0.01 m/s. In addition to the PID controller, the static flow is compensated by adding a uniform magnetic gradient compensating the drag



(a)



(b)

Fig. 16. Navigation within a pipe with a steady flow: (a) imaging and (b) position tracking.

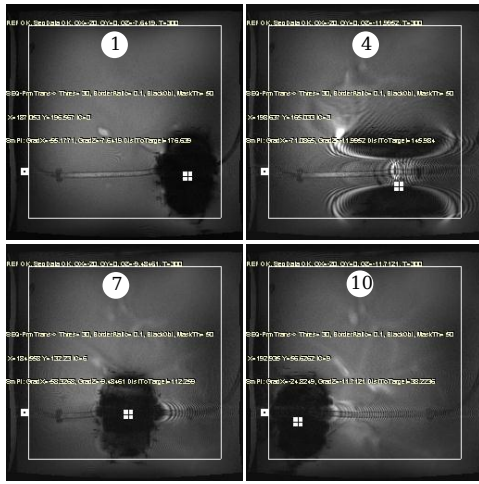
force from the static flow [32]. As shown in Fig.16(a), small fluctuations of the capsule robot are measured through the magnetic artifacts leading to stable position responses of the moving capsule (see Fig.16(b)). Very small fluctuations of the capsule robot can be found.

b) *Pulsatile flow:* In the case of high values of flow rate per stroke (15 cc/stroke) with a pulsating rate leading to a flow velocity of 0.08 m/s, Fig. 17(a) shows magnetic artifacts positions with noticeable error positions. The estimated position differs from the center of gravity of the artifact leading to positioning errors. However, the large fluctuations of the position capsule robot originated from the drag force of the pulsating flow are still measurable. The PID position control with the drag force compensation shows good positioning performance, as shown in Fig.16 17.

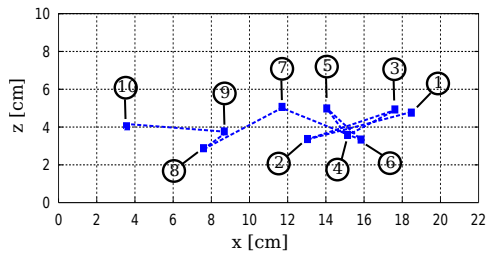
2) *Navigation in a microfluidic vessel simulator:* To assess the propulsion capabilities, an experimental setup has been designed with a Y-shaped branch, as illustrated in Fig.2d. A spherical neodymium (NdFeB-35) bead with a radius of 250 $\mu$ m is then introduced into the channel. A flow of 8 ml/s has been generated using a pulsatile pump, and a gradient perpendicular to the flow switched to assist choosing a branch.

## VI. DISCUSSIONS

In this work, with only a software upgrade, a conventional MRI scanner is improved to perform magnetic resonant navigation (MRN) of ferromagnetic device. A main



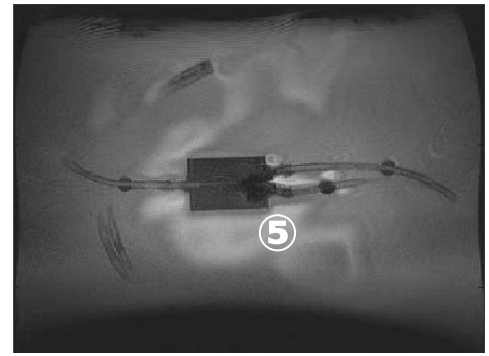
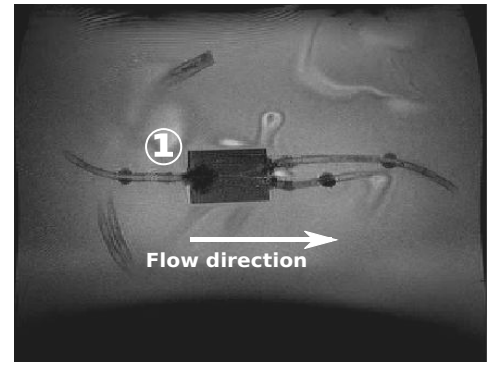
(a)



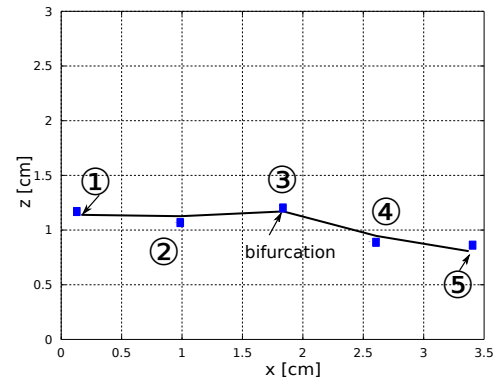
(b)

Fig. 17. Navigation within a pipe in presence of pulsatile flow: (a) imaging and (b) position tracking.

contribution of the present work relies on the reliable 3D MR-tracking based on template matching. MR-tracking approaches for MRN have been first proposed by Martel *et al.* [11], [12], [33]. The approach used employs Magnetic Signature Selective Excitation Tracking (MS-SET) sequence with removed slice selection gradient to perform a projection in all three directions. MS-SET requires the acquisition of three  $k$ -space lines, and then correlation is applied for 3D position determination. In [33] average error of 0.064 mm was achieved for the case of a static particle. In the dynamic case the average error was 1.2 mm. In [11], a static chrome steel sphere with a diameter of 1 mm is localized with a precision of 0.157 mm, whereas a precision of 0.6 mm is obtained in the dynamic case. Recently, the MS-SET has been combined with a passive fiducial marker to improve the procedure efficiency [13]. This extended version of MS-SET offers good accuracy while reducing signal-to noise ratio. With  $k$ -space reduction, our template matching procedure is closely related to MS-SET, and provides similar performance. However, based on common MRI sequence, our MR-tracking framework allows the reconstruction of the surrounding structure (such as the maze structure in Fig. 12a and 13a). Especially, the anatomical structure could be retrieved. It must be noticed that these structures could be recovered only with using a low  $k$ -space reduction, and thus an increase of the acquisition time. To deal with this issue, a solution is to anticipate at the planning stage the evolution of the MR-tracking parameters to increase or decrease the acquisition time as needed. More precisely,



(a)



(b)

Fig. 18. Navigation in Y-shaped microfluidic vessel simulator.

using the information gain map, we can determine locations where high accuracy is needed or less required, and tune the MR-tracking accordingly.

## VII. CONCLUSION

In this paper, we described a framework to extract a robust pathway with respect to MRI-based sensing capabilities. The related dedicated artifact imaging and tracking procedure using a clinical MRI system is presented and evaluated. Sensor feedback for the navigation is extracted by tracking the artifact in the MRI images which are interleaved acquired during sequence execution. From preoperative MRI scan data and the characterized sensing model, a reliable pathway is planned which will be used to control the ferromagnetic microdevices agglomeration through the cardiovascular system to properly reach deep locations in the human body. Each procedure has been experimentally verified using an adapted clinical MRI system. The approaches have shown to be working.

In subsequent steps, the sensing methods have to be combined with a controller and the closed loop control has to be validated over the planned pathway. Also it has to be shown that this approach works in biologically inspired experimental setups.

#### REFERENCES

- [1] Y.-L. Park, S. Elayaperumal, B. Daniel, S. C. Ryu, M. Shin, J. Savall, R. J. Black, B. Moslehi, and M. R. Cutkosky, "Real-time estimation of 3-d needle shape and deflection for mri-guided interventions," *IEEE/ASME Trans. Mechatronics*, vol. 15, no. 6, pp. 906–915, 2010.
- [2] M. Rea, D. McRobbie, H. Elhawary, Z. Tse, M. Lampérth, and I. Young, "System for 3-D real-time tracking of MRI-compatible devices by image processing," *IEEE/ASME Trans. Mechatronics*, vol. 13, no. 3, pp. 379–382, 2008.
- [3] M. Rea, D. McRobbie, H. Elhawary, Z. T. H. Tse, M. Lampérth, and I. Young, "Comparison of mri-compatible mechatronic systems with hydrodynamic and pneumatic actuation," *IEEE/ASME Trans. Mechatronics*, vol. 13, no. 3, pp. 268–277, 2008.
- [4] F. Carpi, A. Khanicheh, C. Mavroidis, and D. De Rossi, "Mri compatibility of silicone-made contractile dielectric elastomer actuators," *IEEE/ASME Trans. Mechatronics*, vol. 13, no. 3, pp. 370–374, 2008.
- [5] J.-B. Mathieu, G. Beaudoin, and S. Martel, "Method of propulsion of a ferromagnetic core in the cardiovascular system through magnetic gradients generated by an mri system," *Biomedical Engineering, IEEE Transactions on*, vol. 53, no. 2, pp. 292–299, 2006.
- [6] J.-H. Park, G. von Maltzahn, L. Zhang, M. P. Schwartz, E. Ruoslahti, S. N. Bhatia, and M. J. Sailor, "Magnetic iron oxide nanoworms for tumor targeting and imaging," *Advanced Materials*, vol. 20, no. 9, pp. 1630–1635, 2008.
- [7] A. Cavalcanti, B. Shirinzadeh, T. Fukuda, and S. Ikeda, "Nanorobot for brain aneurysm," *The International Journal of Robotics Research*, vol. 28, no. 4, pp. 558–570, 2009.
- [8] J. J. Abbott, M. C. Lagomarsino, L. Zhang, L. Dong, and B. J. Nelson, "How should microrobots swim?" *The international journal of Robotics Research*, 2009.
- [9] A. Chanu, O. Felfoul, G. Beaudoin, and S. Martel, "Adapting the clinical mri software environment for real-time navigation of an endovascular untethered ferromagnetic bead for future endovascular interventions," *Magnetic Resonance in medicine*, vol. 59, no. 6, pp. 1287–1297, 2008.
- [10] H. Graf, U. A. Lauer, A. Berger, and F. Schick, "Rf artifacts caused by metallic implants or instruments which get more prominent at 3 t: an in vitro study," *Magnetic resonance imaging*, vol. 23, no. 3, pp. 493–499, 2005.
- [11] O. Felfoul, J.-B. Mathieu, G. Beaudoin, and S. Martel, "In vivo mr-tracking based on magnetic signature selective excitation," *IEEE Trans. Med. Imag.*, vol. 27, no. 1, pp. 28–35, 2008.
- [12] W. Sabra, M. Khouzam, A. Chanu, and S. Martel, "Use of 3d potential field and an enhanced breadth-first search algorithms for the path planning of microdevices propelled in the cardiovascular system," in *27th IEEE EMBS Annual Int. Conf.* IEEE, Apr. 2006, pp. 3916–3920.
- [13] O. Felfoul, A. Becker, C. Bergeles, and P. E. Dupont, "Achieving commutation control of an mri-powered robot actuator," *IEEE Trans. Robot.*, vol. 31, no. 2, pp. 387–399, 2015.
- [14] K. Belharet, D. Folio, and A. Ferreira, "Simulation and planning of a magnetically actuated microrobot navigating in arteries," *IEEE Trans. Biomed. Eng.*, vol. 60, no. 4, pp. 994–1001, Apr. 2013.
- [15] S. Tamaz, R. Gourdeau, A. Chanu, J.-B. Mathieu, and S. Martel, "Real-time mri-based control of a ferromagnetic core for endovascular navigation," *IEEE Trans. Bio-Med. Eng.*, vol. 55, no. 7, pp. 1854–1863, Jul. 2008.
- [16] K. Belharet, D. Folio, and A. Ferreira, "Three-dimensional controlled motion of a microrobot using magnetic gradients," *Advanced Robotics*, vol. 25, no. 8, pp. 1069–1083, 2011.
- [17] L. Arcese, M. Fruchard, and A. Ferreira, "Adaptive controller and observer for a magnetic microrobot," *IEEE Trans. Robot.*, vol. PP, no. 99, pp. 1–8, 2013.
- [18] K. Zhang, F. Maier, A. J. Krafft, R. Umatham, W. Semmler, and M. Bock, "Tracking of an interventional catheter with a ferromagnetic tip using dual-echo projections," *Journal of Magnetic Resonance*, vol. 234, pp. 176–183, 2013.
- [19] J. D. Port and M. G. Pomper, "Quantification and minimization of magnetic susceptibility artifacts on gre images," *Journal of computer assisted tomography*, vol. 24, no. 6, pp. 958–964, 2000.
- [20] D. A. Forsyth and J. Ponce, *Computer Vision: A Modern Approach*. Prentice Hall, 2003.
- [21] T. Wortmann, C. Dahmen, and S. Fatikow, "Study of mri susceptibility artifacts for nanomedical applications," *Journal of Nanotechnology in Engineering and Medicine*, vol. 1, no. 4, p. 041002, 2010.
- [22] K. Belharet, D. Folio, and A. Ferreira, "Endovascular navigation of a ferromagnetic microrobot using MRI-based predictive control," in *IEEE/RSJ Int. Conf. on Intel. Robots and Syst.*, Taipei, Taiwan, Oct. 2010.
- [23] J. A. Sethian, *Level set methods and fast marching methods: evolving interfaces in computational geometry, fluid mechanics, computer vision, and materials science*. Cambridge university press, 1999, vol. 3.
- [24] A. F. Frangi, W. J. Niessen, K. L. Vincken, and M. A. Viergever, "Multiscale vessel enhancement filtering," in *Medical Image Computing and Computer-Assisted InterventionMICCAI98*. Springer, 1998, pp. 130–137.
- [25] Y. Sato, S. Nakajima, N. Shiraga, H. Atsumi, S. Yoshida, T. Koller, G. Gerig, and R. Kikinis, "Three-dimensional multi-scale line filter for segmentation and visualization of curvilinear structures in medical images," *Medical image analysis*, vol. 2, no. 2, pp. 143–168, 1998.
- [26] D. Fox, J. Hightower, L. Liao, D. Schulz, and G. Borriello, "Bayesian filtering for location estimation," *IEEE pervasive computing*, no. 3, pp. 24–33, 2003.
- [27] H. Takeda, C. Facchinetti, and J. Latombe, "Planning the motions of a mobile robot in a sensory uncertainty field," *IEEE Trans. Pattern Anal. Mach. Intell.*, vol. 16, no. 10, pp. 1002–1017, 1994.
- [28] N. Roy and S. Thrun, "Coastal navigation with mobile robots," *Advances in Neural Processing Systems*, vol. 12, no. 12, pp. 1043–1049, 1999.
- [29] H. Takeda and J. Latombe, "Sensory uncertainty field for mobile robot navigation," in *IEEE J Int. Conf. on Intel. Robot. and Autom.*, vol. 3, Nice, France, May 1992, pp. 2465–2472.
- [30] R. He, S. Prentice, and N. Roy, "Planning in information space for a quadrotor helicopter in a GPS-denied environment," in *IEEE J Int. Conf. on Intel. Robot. and Autom.*, 2008, pp. 1814–1820.
- [31] T. Cover, J. Thomas, J. Wiley *et al.*, *Elements of information theory*. Wiley Online Library, 1991, vol. 306.
- [32] J. Choi, S. Jeong, K. Cha, L. Qin, J. Li, J. Park, and S. Park, "Positioning of microrobot in a pulsating flow using ema system," in *IEEE RAS/EMBS Int. Conf. on Biomedical Robotics and Biomechanics (BioRob)*. IEEE, 2010, pp. 588–593.
- [33] E. Aboussouan and S. Martel, "High-precision absolute positioning of medical instruments in mri systems," in *28th IEEE EMBS Annual Int. Conf.* IEEE, 2006, pp. 743–746.